Computational Assessment of I-V Curves and Tunability of 2D Semiconductor van der Waals Heterostructures

NANO LETTERS

pubs.acs.org/NanoLett
Letter

Computational Assessment of *I*–*V* Curves and Tunability of 2D Semiconductor van der Waals Heterostructures

Qiuhua Liang,* Samuel Lara-Avila, Sergey Kubatkin, Md. Anamul Hoque, Saroj Prasad Dash, and Julia Wiktor*

Cite This: *Nano Lett.* 2025, 25, 2052–2058

ABSTRACT: Two-dimensional (2D) transition metal dichalcogenides (TMDs) have received significant interest for use in tunnel field-effect transistors (TFETs) due to their ultrathin layers and tunable band gap features. In this study, we used density functional theory (DFT) to investigate the electronic properties of six TMD heterostructures, namely, $MoSe_2/HfS_2$, $MoTe_2/ZrS_2$, $MoTe_2/HfS_2$, WSe_2/HfS_2, WTe_2/ZrS_2, and WTe_2/HfS_2, focusing on variations in band alignments. We demonstrate that WTe_2/ZrS_2 and WTe_2/HfS_2 have the smallest band gaps (close to 0 or broken) from the considered set. Furthermore, combining DFT with the nonequilibrium Green's function method (DFT-NEGF), we analyzed the output *I*–*V* characteristics, revealing increased current as band gap closes across all studied heterostructures. Notably, WTe_2/ZrS_2 and WTe_2/HfS_2 show a potential negative differential resistance (NDR) even without a broken gap. Importantly, the inclusion of a p-doped gate effect in WTe_2/ZrS_2 enhances the current flow and band-to-band tunneling. The rapidly increasing tunneling current under low applied voltage indicates that the WTe_2/ZrS_2 and WTe_2/HfS_2 heterostructures are promising for applications in TFETs.

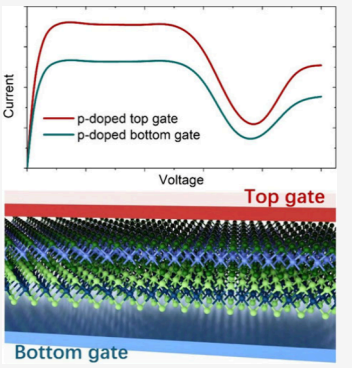

KEYWORDS: *Density Functional Theory (DFT) Calculations, Non-Equilibrium Green Function (NEGF), Transition Metal Dichalcogenide (TMD) Heterostructures, Electronic Transport Property, Tunnel Field-Effect Transistors (TFETs)*

Metal-oxide semiconductor field-effect transistors (MOSFETs) have been the cornerstones of modern electronics for decades. However, MOSFETs face significant disadvantages as device dimensions shrink, particularly in high-density integration. One major issue is the high-power dissipation due to heightened leakage currents and, consequently, power losses as devices are scaled down.[1−3] Additionally, the subthreshold swing limit, governed by the Boltzmann limit, fundamentally challenges the reduction of power consumption.[4−6] In this context, band-to-band tunnel field effect transistors (TFETs) with low energy consumption can potentially be a compelling alternative to break through the subthreshold swing limit by exploiting quantum tunneling mechanisms instead of thermionic emission.[7−9]

Two-dimensional (2D) transition metal dichalcogenide (TMD) materials have gained widespread attention in the field of nanoelectronics due to their atomic scale thickness, mechanical flexibility, band gap tunability, and high conductivity as alternatives to traditional semiconductor materials.[10−13] The 2D van der Waals TMD heterostructures (vdWHs), formed by stacking different layers of 2D TMDs, are highly promising for TFETs due to their fascinating properties beyond traditional bulk material limits. For example, the van der Waals interactions facilitate the assembly of various heterostructures from different materials, circumventing the need for lattice matching that is typical in traditional bulk materials with covalent bonds.[14] Besides, their interfaces are free of dangling bonds and therefore can mitigate the parasitic trap-assisted tunneling current.[15] Importantly, band alignments of these vdWHs can be effectively manipulated by applying an external electric field or adjusting the interlayer distance.[16−21] This flexibility offers the possibility of achieving a broken or near-broken gap alignment, an ideal condition that facilitates band-to-band tunneling with minimal energy loss, which is pivotal for the development of TFETs.

Though some broken or near-broken gap 2D vdWHs formed by combining monolayers of, for instance, $MoSe_2$, WSe_2, $MoTe_2$, WTe_2, ZrS_2, and HfS_2 have been reported using density functional theory (DFT) simulations,[22−24] their electronic transport properties remain largely unexplored. Detailed studies on the electronic transport properties of these vdWHs are expected to provide insights into their potential applications in TFETs. In this study, we systematically investigated the electronic and transport properties of vertically stacked $MoSe_2/HfS_2$, $MoTe_2/ZrS_2$, $MoTe_2/HfS_2$,

Received: November 28, 2024
Revised: January 16, 2025
Accepted: January 17, 2025
Published: January 22, 2025

https://doi.org/10.1021/acs.nanolett.4c06076
Nano Lett. 2025, 25, 2052−2058

WSe_2/HfS_2, WTe_2/ZrS_2, and WTe_2/HfS_2 vdWHs, because of their similar lattice parameters and reported broken or near-broken band gaps.[22,23,25] These characteristics facilitate better structural compatibility and potential applicability to TFET applications. Besides, it has been noted that vertical stacking in vdWH TFET results in a smaller gate-drain capacitance compared to lateral vdWH TFET.[26] We investigated how varying interlayer distances affect the electronic band structures of these vdWHs. Additionally, we systematically analyzed the current−voltage ($I-V$) characteristics of these vdWHs at various interlayer distances, utilizing DFT combined with the nonequilibrium Green's function (DFT-NEGF) calculations. We find that the reduction of the band gap by only 0.03 eV resulted in the increase of the maximum current in the considered voltage range by a factor of 2.62. Interestingly, our findings reveal that the WTe_2/ZrS_2 and WTe_2/HfS_2 heterostructures exhibit negative differential resistance (NDR) behavior, regardless of variations in the band gap, interesting for multivalued logic (MVL) operation. Additionally, we investigate the effects of the gate voltage on WTe_2/ZrS_2. The results indicated that p-type doping can further increase the current and enhance the NDR behavior. This comprehensive study provides a detailed analysis of 2D vdWHs, highlighting their potential for application in TFETs.

Geometry optimizations and electronic structure calculations were performed using the Vienna Ab Initio Simulation Package (VASP) with the projector augmented plane wave (PAW) technique and a plane wave basis set.[27−29] The generalized gradient approximation (GGA) of Perdew, Burke, and Ernzerhof (PBE) was used for the exchange-correlation effects,[30] supplemented by Grimme's DFT-D2 method for van der Waals interactions.[23] A cutoff energy of 500 eV and a Monkhorst−Pack k-point of 9 × 9 × 1 mesh were employed for high accuracy.

SIESTA was utilized to calculate the electronic properties using norm-conserving Troullier−Martin pseudopotentials,[31,32] a double-ζ plus polarization (DZP) basis set within the PBE-GGA functional.[30] This approach was chosen for its ability to provide detailed insights into electronic properties and electron transport calculations, critical to our study.

The electron transport calculations were performed using the DFT combined with the nonequilibrium Green's function (NEGF) method implemented in TranSIESTA.[33] The calculations were aimed at understanding the device physics under operational conditions, using the Landauer−Büttiker formula to compute source-drain current.[34,35] In all of the calculations, spin orbital coupling (SOC) was not included. More details about computation methods can be found in the Supporting Information.

We first relax the monolayers and calculate their electronic band structures. The band structures obtained by using both VASP and SIESTA are given in Figure S1. All the results are in excellent agreement with previously reported theoretical calculations.[22,23,25,36,37] To explore potential interactions that could lead to new or enhanced electronic properties, we construct six different vdWHs from monolayer TMDs, namely, $MoSe_2/HfS_2$, $MoTe_2/ZrS_2$, $MoTe_2/HfS_2$, WSe_2/HfS_2, WTe_2/ZrS_2, and WTe_2/HfS_2. These vdWHs are developed based on the most stable configurations identified in previous studies,[23−25] and the strain is uniformly distributed within the layers when stacked. Additionally, all the lattice mismatches in our studied vdWHs are within 5%.[38,39] The effect of lattice mismatch on the electronic structures of the vdWHs is examined, with band structures calculated using SIESTA and displayed in Figure S3. These results demonstrate that, while lattice mismatch can affect the band structures and band edge positions of the vdWHs, it generally does not alter the overall band alignment. Additionally, the effect of lattice mismatch on the band structure is further analyzed using VASP for the WTe_2/ZrS_2 system, as shown in Figure S4. The band structure obtained from VASP closely matches those calculated from SIESTA, further supporting the conclusion that it is reasonable to disregard the impact of lattice mismatch in these calculations. More details about the effect of lattice mismatch on the $I-V_b$ curve will be discussed below. After construction, each vdWH is optimized to determine the most favorable interlayer distances. The optimized interlayer distances, denoted as "d", were 2.96 Å for $MoSe_2/HfS_2$, 3.10 Å for $MoTe_2/ZrS_2$, 3.09 Å for $MoTe_2/HfS_2$, 2.90 Å for WSe_2/HfS_2, 3.04 Å for WTe_2/ZrS_2, and 3.05 Å for WTe_2/HfS_2, as depicted in Figure 1. The d of all vdWHs is summarized in Table 1.

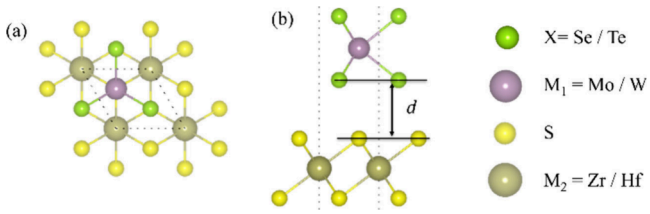

Figure 1. (a) Top and (b) side views of the $M_1X_2-M_2S_2$ vdWHs. d indicates the interlayer distance.

These values are in good agreement with values reported in the literature, further confirming the reliability of our computational setup.[22−25,40,41]

The band structures of the different vdWHs are plotted in Figure 2 with blue lines. All constructed vdWHs from the monolayer TMDs exhibit indirect band gaps. Specifically, the vdWHs $MoSe_2/HfS_2$, $MoTe_2/ZrS_2$, and $MoTe_2/HfS_2$ have relatively small band gaps, while WSe_2/HfS_2, WTe_2/ZrS_2, and WTe_2/HfS_2 show near-broken band gaps. (In this study, we define a near-broken band gap as a band gap that is smaller than 0.1 eV.) The band gap values are as follows: 0.13 eV for $MoSe_2/HfS_2$, 0.18 eV for $MoTe_2/ZrS_2$, 0.19 eV for $MoTe_2/HfS_2$, 0.04 eV for WSe_2/HfS_2, 0.01 eV for WTe_2/ZrS_2, and 0.03 eV for WTe_2/HfS_2. These values are at the level of accuracy that can be expected when comparing DFT calculations with experiment. Therefore, it is important to assess how variations in the band gap, as could be observed experimentally, would impact the transport properties of the vdWHs. The interlayer coupling in vdWHs, strongly influenced by the interlayer distance, significantly affects the electronic structure and physical properties of these materials. Previous studies have demonstrated that reducing the interlayer distance can effectively modify the values of the valence band maximum (VBM) and conduction band minimum (CBM), as well as change the band gaps.[42] Additionally, experiments have demonstrated that adjusting the interlayer distance in these vdWHs is possible by applying hydrostatic pressure.[43] Here we investigated the band structures of these vdWHs at a uniformly reduced d value of 2.70 Å. The results of these investigations are depicted in Figure 2, with red lines. Upon reducing d, the band gaps of $MoSe_2/HfS_2$, $MoTe_2/ZrS_2$, $MoTe_2/HfS_2$, and WSe_2/HfS_2 decreased to 0.06, 0.11, 0.09, and 0.01 eV, respectively, approaching near-broken band gaps. Notably, at a

https://doi.org/10.1021/acs.nanolett.4c06076
Nano Lett. 2025, 25, 2052−2058

Table 1. Interlayer Distances, *d*, of All vdWHs[a]

vdWHs	$MoSe_2/HfS_2$	$MoTe_2/ZrS_2$	$MoTe_2/HfS_2$	WSe_2/HfS_2	WTe_2/ZrS_2	WTe_2/HfS_2
d (Å)	2.96	3.10	3.09	2.90	3.04	3.05
ref.	3.05[40]	3.10[22]	3.14[41]	/	3.10[25]	3.02[23]

[a]The comparison data from other published works are also listed. "/" indicates that no reference was found.

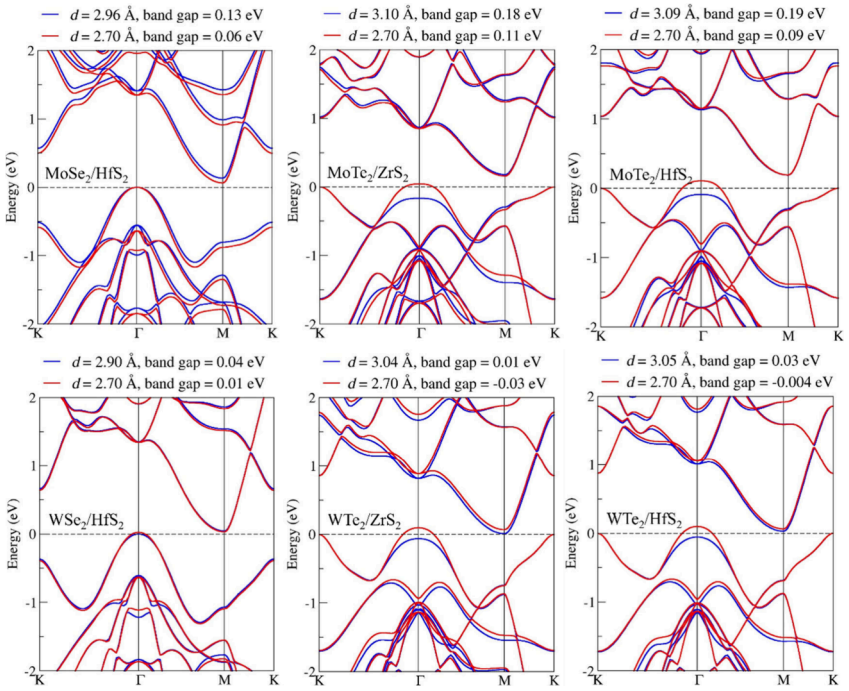

Figure 2. Electronic band structures of vdWHs with different *d* values calculated by SIESTA.

reduced *d* of 2.70 Å, WTe_2/ZrS_2 and WTe_2/HfS_2 exhibit negative band gaps of −0.03 and −0.004 eV. The negative value indicates an energy overlap of 0.03 and 0.004 eV and is characteristic of a broken gap band alignment. It is particularly noteworthy that, in the cases of $MoTe_2/ZrS_2$, $MoTe_2/HfS_2$, WTe_2/ZrS_2, and WTe_2/HfS_2, the reduction in interlayer distance not only affects the band gaps but also precipitates a significant shift in the VBM from the K point to the Γ point. These findings reveal that reducing *d* leads to significant changes in the electronic structures of these vdWHs. This alteration profoundly impacts their band alignments and overall electronic properties, demonstrating the sensitivity of these materials to spatial configuration adjustments.

We then qualitatively investigated the quantum transport properties of these vdWHs with both optimized *d* and standardized *d* of 2.70 Å using the DFT-NEGF method. A two-probe model is constructed to mimic the device, which contains a central scattering region and two semi-infinite electrodes (source and drain), as shown in Figure 3. The entire modeled system contains 336 atoms, with the quantum transport direction occurring between the left and right electrodes. Previous theoretical studies have validated the use of simplified device models to investigate transport properties, confirming their reliability.[25,44−46]

Figure 4 shows the calculated output (I−V_b) characteristics for these vdWHs at both an optimized *d* and a uniform *d* of 2.70 Å. Notably, WTe_2/ZrS_2 exhibits the highest current across all applied voltages among the vdWHs, as illustrated in Figure 4(a). This is followed by WSe_2/HfS_2 and WTe_2/HfS_2. Specifically, WTe_2/ZrS_2 shows a rapid increase to a high

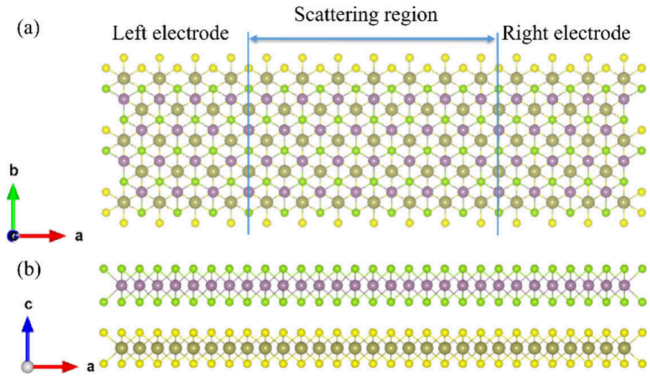

Figure 3. (a) Top and (b) side views of the transport setup with a left electrode, a central scattering region, and a right electrode.

current of 0.54 μA from 0 to 0.1 V. The current then levels off, forming a plateau from approximately 0.1 to 0.5 V, before descending to a valley of 0.34 μA at 0.8 V. The peak-to-valley ratio for this structure is calculated to be 1.59, which is larger than the reported value of 1.00 (1.08) in phosphorene/SnS_2 ($SnSe_2$) vdWHs.[46] Beyond 0.8 V, the current began to rise again. A similar trend is observed in the WTe_2/HfS_2 vdWH, but with a lower peak value of about 0.37 μA at 0.1 V and valley value of 0.26 μA at 0.7 V, resulting in a peak-to-valley ratio of 1.42. Both WTe_2/ZrS_2 and WTe_2/HfS_2 vdWHs display NDR behavior, and the appearance of NDR confirms the presence of band-to-band tunneling (BTBT) transport mechanisms within these structures. In contrast, WSe_2/HfS_2 maintains a steady current of about 0.37 μA across most of the

https://doi.org/10.1021/acs.nanolett.4c06076
Nano Lett. 2025, 25, 2052−2058

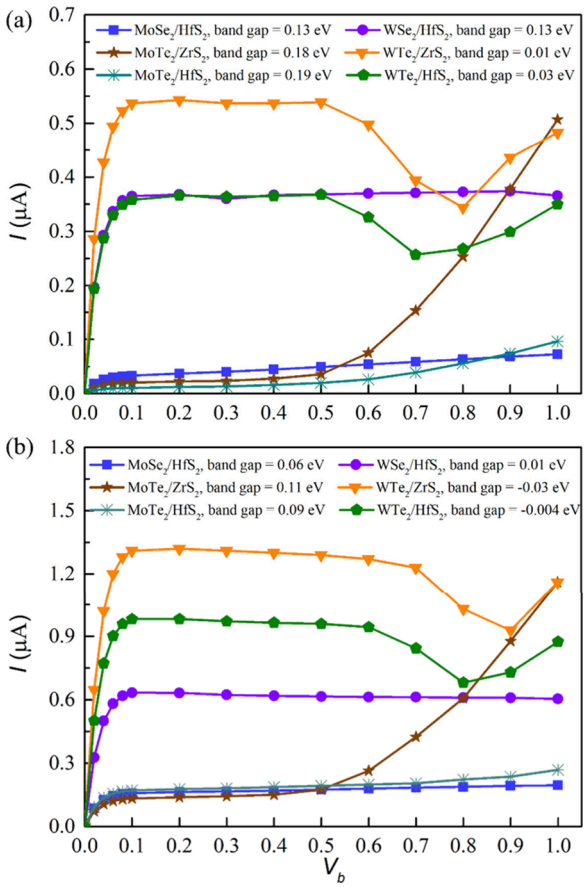

Figure 4. $I-V_b$ curves of the heterostructures with (a) optimized d and (b) d = 2.70 Å.

voltage range, demonstrating a stable electronic response. $MoTe_2/ZrS_2$ remains relatively flat with small current values from 0 to 0.5 V but exhibits a rapid increase after 0.5 V, reaching approximately 0.51 μA at 1.0 V. $MoSe_2/HfS_2$ and $MoTe_2/HfS_2$ consistently exhibit very low currents compared to the others. For $MoSe_2/HfS_2$, $MoTe_2/ZrS_2$, $MoTe_2/HfS_2$, and WSe_2/HfS_2, the NDR behaviors are not observed.

To understand why tungsten-based vdWHs show higher currents than molybdenum-based vdWHs, we perform an analysis of the Bader charge transfer. As shown in Table S1, the overall charge transfer is small due to the weak van der Waals interaction. Nevertheless, tungsten-based vdWHs consistently display charge transfers larger than those of the corresponding molybdenum-based vdWHs. In other words, substituting Mo with W increases the net charge transferred between layers, which is generally associated with stronger electrostatic interactions. Consequently, this enhanced charge transfer boosts the carrier concentration at the interface and thus tailoring of the electronic transport along the interface,[47] thereby improving electrical conductivity and leading to higher current.

Besides, a deeper insight into the observed $I-V_b$ characteristics of $MoTe_2/ZrS_2$ and WTe_2/ZrS_2 vdWHs at optimized d has been analyzed in terms of the behavior of the transmission coefficient. The current in $MoTe_2/ZrS_2$ rises steadily with increasing bias from 0.5 to 0.9 V because more transmission channels enter the bias window, as shown in Figure S5. Conversely, WTe_2/ZrS_2 shows a decrease in current at bias from 0.5 to 0.8 V as its active transmission channels move away from the most relevant energy range, followed by a current increases again at 0.9 V when a new transmission peak appears. More details are discussed in the Supporting Information.

To examine the effect of lattice mismatch on the $I-V_b$ characteristics, we take WTe_2/ZrS_2 as a case study and calculate its $I-V_b$ with 5% compression in the lattice. The results, displayed in Figure S6, indicate that compressing the lattice constants leads to a larger current than the uncompressed system at the same applied voltage. The maximum current reached approximately 0.98 μA between 0.1 and 0.3 V, and the minimum current was about 0.62 μA at V_b = 0.7 V. Despite the compression, the system still exhibits a similar trend to the uncompressed setup, displaying NDR behavior with a peak-to-valley ratio of 1.58. Thus, these findings suggest that the lattice mismatch does not alter our initial conclusions.

After reducing d, and therefore the band gaps, the vdWHs show similar current trends as observed with optimized d, as illustrated in Figure 4b. Notably, Figure 4b generally shows higher current outputs across all vdWHs compared with Figure 4a. Specifically, WTe_2/ZrS_2 demonstrates a sharp increase from 0 to 0.1 V with a peak value of about 1.32 μA, maintaining a plateau from approximately 0.1 to 0.7 V, before reaching a valley value of 0.93 μA at 0.9 V. The peak-to-valley ratio is calculated to be 1.42. NDR behavior is observed when V_b exceeds 0.6 V and dissipates above 0.9 V. For WTe_2/HfS_2, the current also increases rapidly from 0 to 0.1 V, achieving a maximum of about 0.97 μA, with a plateau extending from around 0.1 to 0.6 V, and reaching a valley value of 0.68 μA at 0.8 V. NDR behavior is similarly noted for V_b beyond 0.6 V and is lost after 0.8 V, with a peak-to-valley ratio of 1.43.

The other structures, $MoSe_2/HfS_2$, $MoTe_2/ZrS_2$, $MoTe_2/HfS_2$, and WSe_2/HfS_2, still do not exhibit NDR behavior but show higher current outputs compared to those at optimized d. Specifically, WSe_2/HfS_2 maintains a steady current of about 0.62 μA across most of the voltage range. The $I-V_b$ curve of $MoTe_2/ZrS_2$ remains relatively flat with low current values from 0 to 0.5 V but experiences a notable rise after 0.5 V, reaching about 1.16 μA at V_b of 1.0 V. Both $MoSe_2/HfS_2$ and $MoTe_2/HfS_2$ continue to exhibit low currents throughout the entire V_b range compared to the other structures.

The observed increase in current, consistent with the decreases in the band gaps of the vdWHs, reflects the significant influence of interlayer compression on the electronic transport properties. Interlayer compression may enhance interlayer coupling in vdWHs, thus leading to a reduction in the band gaps and an increase in current. The exceptional transport performance of WTe_2/ZrS_2 and WTe_2/HfS_2 vdWHs, characterized by rapid current increases within 0.1 V and evident NDR behaviors, highlights their potential for application in TFETs.

Finally, we simulated the effect of gate voltage on the transport property of WTe_2/ZrS_2 at optimized d by introducing a specific fixed charge in the system, ensuring the total charge in the system remained zero.[48−50] Both positive (p-type) and negative (n-type) doping are considered, with a doping concentration of 1.39×10^{13} cm^{-2}.[50] For each type of doping, both the top gate and bottom gate are analyzed, respectively, as depicted in Figure 5a.

In Figure 5b, we present the calculated $I-V_b$ curves for both p-type and n-type doping at the top gate and bottom gate configurations. After doping, the current can further increase compared to the undoped system. And like the undoped WTe_2/ZrS_2 system, the $I-V_b$ curves of the p-doped $WTe_2/$

https://doi.org/10.1021/acs.nanolett.4c06076
Nano Lett. 2025, 25, 2052−2058

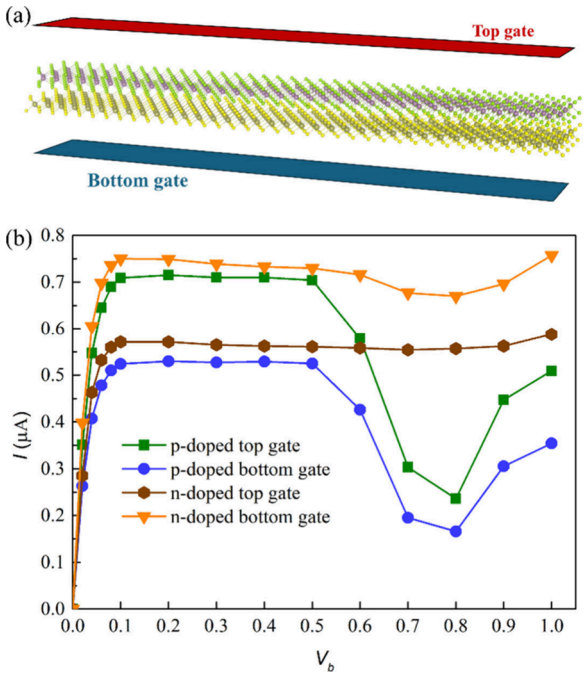

Figure 5. (a) Schematic diagram of applying the bottom gate and top gate on the device and (b) $I-V_b$ curves of p-doped and n-doped WTe_2/ZrS_2 at the optimized d.

ZrS_2 system show evident NDR behavior. Specifically, in the p-type doped top gate system (green line), there is an enhanced current compared to the undoped system, with the current increasing sharply from 0 to 0.1 V and peaking at 0.71 μA, before reaching a valley of 0.24 μA at 0.8 V. NDR behavior is observed for $V_b > 0.5$ V and disappears above 0.8 V. The peak-to-valley ratio increases to 2.96, which is comparable to the recent experimental value of approximately 3 found in $MoTe_2/SnS_2$.[21] In the p-type doped bottom gate system (blue line), the current also increases sharply from 0 to 0.1 V with a peak of 0.52 μA and reaches a valley of 0.17 μA at 0.8 V. Here too, NDR behavior is evident for $V_b > 0.5$ V and vanishes above 0.8 V. The peak-to-valley ratio in this configuration is calculated to be 3.06. The larger peak-to-valley ratio in both p-doped systems compared to the undoped system suggests that more pronounced BTBT behavior may occur in the p-doped system.

Conversely, the n-doped systems do not exhibit significant or any NDR behavior. In the n-type doped top gate system (brown line), the current rises to 0.57 μA at $V_b = 0.1$ V and maintains a steady value at $V_b > 0.1$ V, with no NDR behavior observed. In the n-type doped bottom gate system (orange line), the current peaks at 0.75 μA at $V_b = 0.1$ V and slightly decreases to 0.67 μA at $V_b = 0.8$ V, before increasing again after $V_b > 0.8$ V, with a peak-to-valley ratio of 1.12; the NDR behavior here is not as evident as in the undoped and p-doped systems. When applying different gate doping, the different interlayer polarizations and the electric field direction across the semiconductor channel may result in the different $I-V_b$ characteristics.[51] The peak-to-valley ratios of WTe_2/ZrS_2 without and with a gate voltage effect are summarized in Table 2.

Besides, we investigated the effect of a p-doped bottom gate on WTe_2/ZrS_2 as a case study to assess how gate strength influences the peak-to-valley ratio in the NDR behavior. Concentrations of 1.39×10^{13} and 0.56×10^{13} cm^{-2} are shown

Table 2. Peak-to-Valley Ratio of WTe_2/ZrS_2 without and with the Gate Voltage Effect

WTe_2/ZrS_2	without gate effect	p-doped top gate	p-doped bottom gate	n-doped top gate	n-doped bottom gate
peak-to-valley ratio	1.59	2.96	3.06	1	1.12

in Figure S7. The results demonstrate that the strength of the gate effect can significantly affect the peak-to-valley ratio. Lower doping concentration results in a lower maximum current. Specifically, the system with 0.56×10^{13} cm^{-2} exhibits a peak-to-valley ratio of 2.08, which is lower than the 1.39×10^{13} cm^{-2} system with a peak-to-valley ratio of 3.06. Thus, a stronger gate effect results in a higher maximum current and a higher peak-to-valley ratio.

We note that our calculations do not include the SOC. This effect will result in the splitting at the VBM of TMDs.[52] To determine the effect of SOC on the electronic structures of vdWHs, we chose WTe_2/ZrS_2 as a case study. The band structures were calculated using PBE and PBE0, with and without SOC, performed in VASP and displayed in Figure S8. Due to error cancellation, we find that PBE and PBE0+SOC exhibit the same extent of the broken gap. Considering the accuracy of the band gap and the significantly increased computational demands of using PBE0+SOC, we opted not to include SOC in our primary calculations and used PBE instead. More details are available in the Supporting Information.

Overall, the p-doped top gate system shows enhanced current and NDR behavior, the p-doped bottom gate system shows enhanced NDR behavior, and the n-type doped systems primarily show enhancements in current but not NDR behavior. These findings highlight the critical influence of the gate voltage on the electronic transport properties of vdWHs, providing valuable insights into the design and optimization of TFETs.

In conclusion, we combined density functional theory (DFT) with nonequilibrium Green's function (NEGF) methods to investigate the electronic and transport properties of $MoSe_2/HfS_2$, $MoTe_2/ZrS_2$, $MoTe_2/HfS_2$, WSe_2/HfS_2, WTe_2/ZrS_2, and WTe_2/HfS_2 heterostructures. We assessed the effects of reducing interlayer distances on the band structures of these heterostructures, highlighting the reduction of band gaps and the emergence of broken gaps in WTe_2/ZrS_2 and WTe_2/HfS_2. The $I-V$ characteristics calculated for these heterostructures show increased current with a decreased band gap. Notably, WTe_2/ZrS_2 and WTe_2/HfS_2 demonstrate sharp increases in current within low applied voltage and the negative differential resistance (NDR) behavior across various distances. A slight reduction in the band gap by just 0.03 eV results in an increase in the maximum current within the considered voltage range—by factors of 2.44 and 2.62 for WTe_2/ZrS_2 and WTe_2/HfS_2, respectively. Importantly, we also considered the gate effect and found that the p-doped gate effect can further increase the current and enhance the band-to-band tunneling behavior. Our findings suggest that achieving a broken band gap in heterostructures is challenging; however, minimizing the band gap, even if it is not fully broken, remains a crucial objective due to its potential to enhance electronic properties.

https://doi.org/10.1021/acs.nanolett.4c06076
Nano Lett. 2025, 25, 2052−2058

■ ASSOCIATED CONTENT

Supporting Information

The Supporting Information is available free of charge at https://pubs.acs.org/doi/10.1021/acs.nanolett.4c06076.

Computational details, band structures calculated by VASP and SIESTA, k-point test results (WSe_2/HfS_2), lattice mismatch effects (vdWHs, SIESTA), band structures (WTe_2/ZrS_2, +5% and no compression, VASP), Bader charge analysis (all vdWHs), transmission coefficients ($MoTe_2/ZrS_2$, WTe_2/ZrS_2, various voltages), $I-V$ curves (WTe_2/ZrS_2, +5% and no compression, p-doping), and comparison of hybrid functional and SOC effects on band structure (WTe_2/ZrS_2) (PDF)

■ AUTHOR INFORMATION

Corresponding Authors

Qiuhua Liang − *Department of Physics, Chalmers University of Technology, SE-412 96 Gothenburg, Sweden;* orcid.org/0000-0002-5436-5203; Email: qiuhua.liang@chalmers.se

Julia Wiktor − *Department of Physics, Chalmers University of Technology, SE-412 96 Gothenburg, Sweden;* orcid.org/0000-0003-3395-1104; Email: julia.wiktor@chalmers.se

Authors

Samuel Lara-Avila − *Department of Microtechnology and Nanoscience, Chalmers University of Technology, SE-412 96 Gothenburg, Sweden;* orcid.org/0000-0002-8331-718X

Sergey Kubatkin − *Department of Microtechnology and Nanoscience, Chalmers University of Technology, SE-412 96 Gothenburg, Sweden;* orcid.org/0000-0001-8551-9247

Md. Anamul Hoque − *Department of Microtechnology and Nanoscience, Chalmers University of Technology, SE-412 96 Gothenburg, Sweden;* orcid.org/0000-0002-2117-7177

Saroj Prasad Dash − *Department of Microtechnology and Nanoscience, Chalmers University of Technology, SE-412 96 Gothenburg, Sweden;* orcid.org/0000-0001-7931-4843

Complete contact information is available at: https://pubs.acs.org/10.1021/acs.nanolett.4c06076

Notes

The authors declare no competing financial interest.

■ ACKNOWLEDGMENTS

We acknowledge funding from the Swedish Strategic Research Foundation through a Future Research Leader program (FFL21-0129), the Chalmers Area of Advance − Energy, and the 2D TECH VINNOVA Competence Center (No. 2019-00068). For the computations we used resources provided by the Swedish National Infrastructure for Computing (SNIC) at NSC and C3SE.

■ REFERENCES

(1) Natori, K. Ballistic metal-oxide-semiconductor field effect transistor. *J. Appl. Phys.* **1994**, *76* (8), 4879−4890.

(2) Lee, M. L.; Fitzgerald, E. A.; Bulsara, M. T.; Currie, M. T.; Lochtefeld, A. Strained Si, SiGe, and Ge channels for high-mobility metal-oxide-semiconductor field-effect transistors. *J. Appl. Phys.* **2005**, *97* (1), 011101.

(3) Ferain, I.; Colinge, C. A.; Colinge, J.-P. Multigate transistors as the future of classical metal-oxide-semiconductor field-effect transistors. *Nature* **2011**, *479* (7373), 310−316.

(4) Chaudhry, A.; Kumar, M. J. Controlling short-channel effects in deep-submicron SOI MOSFETs for improved reliability: a review. *IEEE Trans. Device Mater. Reliab.* **2004**, *4* (1), 99−109.

(5) Adan, A. O.; Tanaka, D.; Burgyan, L.; Kakizaki, Y. The current status and trends of 1,200-V commercial silicon-carbide MOSFETs: Deep physical analysis of power transistors from a designer's perspective. *IEEE Power Electron. Mag.* **2019**, *6* (2), 36−47.

(6) Sarkar, A.; Das, A. K.; De, S.; Sarkar, C. K. Effect of gate engineering in double-gate MOSFETs for analog/RF applications. *Microelectr. J.* **2012**, *43* (11), 873−882.

(7) Ionescu, A. M.; Riel, H. Tunnel field-effect transistors as energy-efficient electronic switches. *Nature* **2011**, *479* (7373), 329−337.

(8) Sarkar, D.; Xie, X.; Liu, W.; Cao, W.; Kang, J.; Gong, Y.; Kraemer, S.; Ajayan, P. M.; Banerjee, K. A subthermionic tunnel field-effect transistor with an atomically thin channel. *Nature* **2015**, *526* (7571), 91−95.

(9) Lu, H.; Seabaugh, A. Tunnel field-effect transistors: State-of-the-art. *IEEE J. Electron Devices Soc.* **2014**, *2* (4), 44−49.

(10) Choi, W.; Choudhary, N.; Han, G. H.; Park, J.; Akinwande, D.; Lee, Y. H. Recent development of two-dimensional transition metal dichalcogenides and their applications. *Mater. Today* **2017**, *20* (3), 116−130.

(11) Duan, X.; Wang, C.; Pan, A.; Yu, R.; Duan, X. Two-dimensional transition metal dichalcogenides as atomically thin semiconductors: opportunities and challenges. *Chem. Soc. Rev.* **2015**, *44* (24), 8859−8876.

(12) Jariwala, D.; Sangwan, V. K.; Lauhon, L. J.; Marks, T. J.; Hersam, M. C. Emerging device applications for semiconducting two-dimensional transition metal dichalcogenides. *ACS Nano* **2014**, *8* (2), 1102−1120.

(13) Meng, R.; Jiang, J.; Liang, Q.; Yang, Q.; Tan, C.; Sun, X.; Chen, X. Design of graphene-like gallium nitride and WS 2/WSe 2 nanocomposites for photocatalyst applications. *Sci. China Mater.* **2016**, *59*, 1027−1036.

(14) Frisenda, R.; Navarro-Moratalla, E.; Gant, P.; De Lara, D. P.; Jarillo-Herrero, P.; Gorbachev, R. V.; Castellanos-Gomez, A. Recent progress in the assembly of nanodevices and van der Waals heterostructures by deterministic placement of 2D materials. *Chem. Soc. Rev.* **2018**, *47* (1), 53−68.

(15) Lim, J. Y.; Kim, M.; Jeong, Y.; Ko, K. R.; Yu, S.; Shin, H. G.; Moon, J. Y.; Choi, Y. J.; Yi, Y.; Kim, T. Van der Waals junction field effect transistors with both n-and p-channel transition metal dichalcogenides. *npj 2D Mater. Appl.* **2018**, *2* (1), 37.

(16) Roy, T.; Tosun, M.; Cao, X.; Fang, H.; Lien, D.-H.; Zhao, P.; Chen, Y.-Z.; Chueh, Y.-L.; Guo, J.; Javey, A. Dual-gated MoS2/WSe2 van der Waals tunnel diodes and transistors. *ACS Nano* **2015**, *9* (2), 2071−2079.

(17) Roy, T.; Tosun, M.; Hettick, M.; Ahn, G. H.; Hu, C.; Javey, A. 2D-2D tunneling field-effect transistors using $WSe_2/SnSe_2$ heterostructures. *Appl. Phys. Lett.* **2016**, *108* (8), 083111.

(18) Komsa, H.-P.; Krasheninnikov, A. V. Electronic structures and optical properties of realistic transition metal dichalcogenide heterostructures from first principles. *Phys. Rev. B* **2013**, *88* (8), 085318.

(19) Rigosi, A. F.; Hill, H. M.; Li, Y.; Chernikov, A.; Heinz, T. F. Probing interlayer interactions in transition metal dichalcogenide heterostructures by optical spectroscopy: MoS2/WS2 and MoSe2/WSe2. *Nano Lett.* **2015**, *15* (8), 5033−5038.

(20) Ghosh, S.; Varghese, A.; Jawa, H.; Yin, Y.; Medhekar, N. V.; Lodha, S. Polarity-tunable photocurrent through band alignment engineering in a high-speed WSe2/SnSe2 diode with large negative responsivity. *ACS Nano* **2022**, *16* (3), 4578−4587.

(21) Mitra, R.; Iordanidou, K.; Shetty, N.; Hoque, M. A.; Datta, A.; Kalaboukhov, A.; Wiktor, J.; Kubatkin, S.; Dash, S. P.; Lara-Avila, S. Gate-tunable negative differential resistance in multifunctional van der Waals heterostructure. *arXiv*, 2024. DOI: 10.48550/arXiv.2409.04908 (accessed September 7, 2024).

(22) Iordanidou, K.; Wiktor, J. Two-dimensional Mo Te 2/Sn Se 2 van der Waals heterostructures for tunnel-FET applications. *Physical Review Materials* **2022**, *6* (8), 084001.
(23) Lei, C.; Ma, Y.; Xu, X.; Zhang, T.; Huang, B.; Dai, Y. Broken-gap type-III band alignment in WTe_2/HfS_2 van der Waals heterostructure. *J. Phys. Chem. C* **2019**, *123* (37), 23089−23095.
(24) Ataei, S. S.; Sadeghi, A. Robust broken-gap $MoTe_2/ZrS_2$ van der Waals heterostructure. *Phys. Rev. B* **2022**, *106* (24), 245301.
(25) Guo, Z.; Hu, K.; Su, J.; Chen, J.; Dong, H.; Pan, M.; Nie, Z.; Wu, F. Tunable electronic properties and negative differential resistance effect of the intrinsic type-III ZrS2/WTe2 van der Waals heterostructure. *Appl. Surf. Sci.* **2023**, *611*, 155644.
(26) Li, M. O.; Yan, R.; Jena, D.; Xing, H. G. Two-dimensional heterojunction interlayer tunnel FET (Thin-TFET): From theory to applications; 2016 IEEE International Electron Devices Meeting (IEDM); IEEE: 2016; pp 19.2.1−19.2.4.
(27) Blöchl, P. E. Projector augmented-wave method. *Phys. Rev. B* **1994**, *50* (24), 17953.
(28) Kresse, G.; Joubert, D. From ultrasoft pseudopotentials to the projector augmented-wave method. *Phys. Rev. B* **1999**, *59* (3), 1758.
(29) Kresse, G.; Furthmüller, J. Efficient iterative schemes for ab initio total-energy calculations using a plane-wave basis set. *Phys. Rev. B* **1996**, *54* (16), 11169.
(30) Perdew, J. P.; Burke, K.; Ernzerhof, M. Generalized gradient approximation made simple. *Phys. Rev. Lett.* **1996**, *77* (18), 3865.
(31) Soler, J. M.; Artacho, E.; Gale, J. D.; García, A.; Junquera, J.; Ordejón, P.; Sánchez-Portal, D. The SIESTA method for ab initio order-N materials simulation. *J. Condens. Matter Phys.* **2002**, *14* (11), 2745.
(32) Troullier, N.; Martins, J. L. Efficient pseudopotentials for plane-wave calculations. *Phys. Rev. B* **1991**, *43* (3), 1993.
(33) Brandbyge, M.; Mozos, J.-L.; Ordejón, P.; Taylor, J.; Stokbro, K. Density-functional method for nonequilibrium electron transport. *Phys. Rev. B* **2002**, *65* (16), 165401.
(34) Datta, S. *Electronic transport in mesoscopic systems*; Cambridge University Press: Cambridge, England, 1997.
(35) van den Broek, B.; Houssa, M.; Iordanidou, K.; Pourtois, G.; Afanas'ev, V.; Stesmans, A. Functional silicene and stanene nanoribbons compared to graphene: electronic structure and transport. *2D Mater.* **2016**, *3* (1), 015001.
(36) Koda, D. S.; Bechstedt, F.; Marques, M.; Teles, L. K. Tuning electronic properties and band alignments of phosphorene combined with $MoSe_2$ and WSe_2. *J. Phys. Chem. C* **2017**, *121* (7), 3862−3869.
(37) Kumar, S.; Schwingenschlogl, U. Thermoelectric response of bulk and monolayer MoSe2 and WSe2. *Chem. Mater.* **2015**, *27* (4), 1278−1284.
(38) Zheng, H.; Li, X.-B.; Chen, N.-K.; Xie, S.-Y.; Tian, W. Q.; Chen, Y.; Xia, H.; Zhang, S.; Sun, H.-B. Monolayer II-VI semiconductors: A first-principles prediction. *Phys. Rev. B* **2015**, *92* (11), 115307.
(39) Hu, J.; Duan, W.; He, H.; Lv, H.; Huang, C.; Ma, X. A promising strategy to tune the Schottky barrier of a $MoS_{2(1-x)}Se_{2x}$/graphene heterostructure by asymmetric Se doping. *J. Mater. Chem. C* **2019**, *7* (25), 7798−7805.
(40) Wang, B.; Wang, X.; Wang, P.; Yang, T.; Yuan, H.; Wang, G.; Chen, H. Bilayer MoSe2/HfS2 nanocomposite as a potential visible-light-driven z-scheme photocatalyst. *Nanomaterials* **2019**, *9* (12), 1706.
(41) Wang, B.; Wang, X.; Wang, P.; Kuang, A.; Zhou, T.; Yuan, H.; Chen, H. Bilayer MoTe2/XS2 (X= Hf, Sn, Zr) heterostructures with efficient carrier separation and light absorption for photocatalytic water splitting into hydrogen. *Appl. Surf. Sci.* **2021**, *544*, 148842.
(42) Wang, Q.; Liang, Y.; Yao, H.; Li, J.; Wang, B.; Wang, J. Emerging negative differential resistance effects and novel tunable electronic behaviors of the broken-gap $KAgSe/SiC_2$ van der Waals heterojunction. *J. Mater. Chem. C* **2020**, *8* (24), 8107−8119.
(43) Fülöp, B.; Márffy, A.; Tóvári, E.; Kedves, M.; Zihlmann, S.; Indolese, D.; Kovács-Krausz, Z.; Watanabe, K.; Taniguchi, T.; Schönenberger, C. New method of transport measurements on van der Waals heterostructures under pressure. *J. Appl. Phys.* **2021**, *130* (6), 064303.
(44) Xie, S.; Jin, H.; Li, J.; Wei, Y. Promises of main-group metal chalcogenide-based broken-gap van der waals heterojunctions for tunneling field effect transistors. *ACS Appl. Electron. Mater.* **2021**, *3* (2), 898−904.
(45) Fang, L.; Wang, T.; Li, J.; Xia, C.; Li, X. Band structures and transport properties of broken-gap heterostructures: 2D C3N/MX case. *Carbon* **2023**, *202*, 119−127.
(46) Xia, C.; Du, J.; Li, M.; Li, X.; Zhao, X.; Wang, T.; Li, J. Effects of Electric Field on the Electronic Structures of Broken-gap Phosphorene/SnX_2 (X= S, Se) van der Waals Heterojunctions. *Phys. Rev. Appl.* **2018**, *10* (5), 054064.
(47) Gunkel, F.; Christensen, D. V.; Pryds, N. Charge-transfer engineering strategies for tailored ionic conductivity at oxide interfaces. *J. Mater. Chem. C* **2020**, *8* (33), 11354−11359.
(48) Stradi, D.; Papior, N. R.; Hansen, O.; Brandbyge, M. Field Effect in graphene-based van der Waals heterostructures: Stacking sequence matters. *Nano Lett.* **2017**, *17* (4), 2660−2666.
(49) Papior, N.; Gunst, T.; Stradi, D.; Brandbyge, M. Manipulating the voltage drop in graphene nanojunctions using a gate potential. *Phys. Chem. Chem. Phys.* **2016**, *18* (2), 1025−1031.
(50) Urquiza, M. L.; Cartoixà, X. Schottky barriers, emission regimes and contact resistances in 2H-1T'MoS2 lateral metal-semiconductor junctions from first-principles. *2D Mater.* **2020**, *7* (4), 045030.
(51) Li, Y.; Li, F.; Chen, Z. Graphane/fluorographene bilayer: considerable C-H··· F-C hydrogen bonding and effective band structure engineering. *J. Am. Chem. Soc.* **2012**, *134* (27), 11269−11275.
(52) Cheng, Y.; Zhu, Z.; Tahir, M.; Schwingenschlögl, U. Spin-orbit-induced spin splittings in polar transition metal dichalcogenide monolayers. *Europhys. Lett.* **2013**, *102* (5), 57001.

https://doi.org/10.1021/acs.nanolett.4c06076
Nano Lett. 2025, 25, 2052−2058